High-Performance Coherent Population Trapping Clock with Polarization Modulation

Peter Yun,[1,*] François Tricot,[1] Claudio Eligio Calosso,[2] Salvatore Micalizio,[2] Bruno François,[3] Rodolphe Boudot,[3] Stéphane Guérandel,[1] and Emeric de Clercq[1]

[1]*LNE-SYRTE, Observatoire de Paris, PSL Research University, CNRS, Sorbonne Universités, UPMC Univ. Paris 06, 61 avenue de l'Observatoire, 75014 Paris, France*

[2]*Istituto Nazionale di Ricerca Metrologica, INRIM, Strada delle Cacce 91, 10135 Torino, Italy*

[3]*FEMTO-ST, CNRS, UBFC, 26 chemin de l'Épitaphe 25030 Besançon Cedex, France*

(Received 1 October 2016; revised manuscript received 25 December 2016; published 25 January 2017)

We demonstrate a vapor-cell atomic-clock prototype based on a continuous-wave interrogation and double-modulation coherent population trapping (DM-CPT) technique. The DM-CPT technique uses a synchronous modulation of polarization and the relative phase of a bichromatic laser beam in order to increase the number of atoms trapped in a dark state, i.e., a nonabsorbing state. The narrow resonance, observed in the transmission of a Cs vapor cell, is used as a narrow frequency discriminator in an atomic clock. A detailed characterization of the CPT resonance versus numerous parameters is reported. A short-term fractional-frequency stability of $3.2 \times 10^{-13}\tau^{-1/2}$ up to a 100-s averaging time is measured. These performances are more than one order of magnitude better than industrial Rb clocks and are comparable to those of the best laboratory-prototype vapor-cell clocks. The noise-budget analysis shows that the short- and midterm frequency stability is mainly limited by the power fluctuations of the microwave used to generate the bichromatic laser. These preliminary results demonstrate that the DM-CPT technique is well suited for the development of a high-performance atomic clock, with the potential compact and robust setup due to its linear architecture. This clock could find future applications in industry, telecommunications, instrumentation, or global navigation satellite systems.

DOI: 10.1103/PhysRevApplied.7.014018

I. INTRODUCTION

Microwave Rb vapor-cell atomic clocks [1], based on optical-microwave double resonance, are today ubiquitous timing devices used in numerous fields of industry, including instrumentation, telecommunications, and satellite-based navigation systems. Their success is explained by their ability to demonstrate excellent short-term fractional-frequency stability at the level of $10^{-11}\tau^{-1/2}$, combined with a small size, weight, and power consumption and a relatively modest cost. Over the past decade, the use of narrow-linewidth semiconductor lasers and the demonstration of advanced atom interrogation techniques, has led to the development in laboratories of new-generation vapor-cell clocks [2–5]. For instance, the pulsed-optical-pumping clock uses a pulsed microwave interrogation, together with a pulsed pumping and detection. Such clocks have achieved a 100-fold improvement in frequency stability compared to existing commercial vapor-cell clocks.

Among the clocks based on advanced interrogation techniques, clocks based on a quantum-interference phenomenon named coherent population trapping (CPT) have proven to be promising alternative candidates. Since its discovery in 1976 [6], coherent population trapping physics [7–10] has motivated stimulating studies in various fields covering fundamental and applied physics such as slow-light experiments [11], high-resolution laser spectroscopy, magnetometers [12,13], laser cooling [14], or atomic frequency standards. Basically, CPT occurs by connecting two long-lived ground-state hyperfine levels of an atomic species to a common excited state by the simultaneous action of two resonant optical fields. When both optical fields are resonant or close to the resonance, and at null Raman detuning—i.e., when the frequency difference between both optical fields matches perfectly the atomic ground-state hyperfine frequency—atoms are trapped through a destructive quantum-interference process into a noninteracting coherent superposition of both ground states, the so-called dark state, resulting in a clear decrease of the light absorption or, equivalently, in a net increase of the transmitted light. The output resonance signal, whose linewidth is ultimately limited by the CPT coherence lifetime, can then be used as a narrow frequency discriminator towards the development of an atomic frequency standard. In a CPT-based clock, unlike the traditional double-resonance Rb clock [15], the microwave signal used to probe the hyperfine frequency is directly optically carried, allowing us to remove the microwave cavity and, potentially, to significantly shrink the clock dimensions.

The application of CPT to atomic clocks was first demonstrated in a sodium atomic beam [16,17]. In 1993, Cyr *et al.* proposed a simple method to produce a microwave clock transition in a vapor cell with purely optical means by using a modulated diode laser [18], demonstrating its high

*enxue.yun@obspm.fr, yunenxue@163.com

potential for compactness. In 2001, a first remarkably compact atomic-clock prototype was demonstrated in NIST [19,20]. Further integration was achieved later thanks to the proposal [21] and development of microfabricated alkali vapor cells [22], leading to the demonstration of the first chip-scale atomic-clock prototype (CSAC) [23] and, later, to the first commercially available CSAC [24]. Nevertheless, this extreme miniaturization effort induces a typical fractional-frequency stability limited at the level of $10^{-10}\tau^{-1/2}$, not compliant with dedicated domains requiring better stability performances. In that sense, in the frame of the European collaborative Mclocks project [25], significant efforts have been pursued to demonstrate compact (i.e., a centimeter-scale cell instead of the millimeter-scale one found in the CSAC) high-performance CPT-based atomic clocks and to help to push this technology to industry.

In standard CPT clocks, a major limitation in reaching better frequency-stability performances is the low contrast (C, the amplitude-to-background ratio) of the detected CPT resonance. This low contrast is explained by the fact that atoms interact with a circularly polarized bichromatic laser beam, leading most of the atomic population into extreme Zeeman sublevels of the ground state, the so-called end states. Several optimized CPT pumping schemes, aiming to maximize the number of atoms participating in the clock transition (the 0-0 magnetically insensitive transition), have been proposed in the literature to circumvent this issue (see Refs. [26,27] and the references therein), but at the expense of increased complexity.

In that sense, an alternative constructive polarization modulation CPT [28] pumping technique, named the double-modulation (DM) scheme, was recently proposed. It consists of applying a phase modulation between both optical components of the bichromatic laser synchronously with a polarization modulation. The phase modulation is needed to ensure a dark state common to both polarizations, allowing us to pump a maximum number of atoms into the desired magnetic-field-insensitive clock state. Compared to the push-pull optical pumping [29–31] or the lin ⊥ lin technique [32,33], this elegant solution presents the main advantage of avoiding any optical beam separation or superposition and is consequently well adapted to provide a compact and robust linear architecture setup.

In this article, we demonstrate a high-performance cw-regime CPT clock based on the DM technique. Optimization of the short-term frequency stability is performed by careful characterization of the CPT resonance versus relevant experimental parameters. A short-term frequency stability at the level of $3.2 \times 10^{-13}\tau^{-1/2}$, up to 100 s, comparable to the best vapor-cell frequency standards, is reported. A detailed noise budget is given, highlighting a dominant contribution of the microwave-power fluctuations. Section II describes the experimental setup. Section III reports the detailed CPT resonance spectroscopy versus experimental parameters. Section IV reports the best short-term frequency-stability results. Noise sources limiting stability are carefully analyzed. In Sec. V, we study the clock-frequency shift versus each parameter and estimate the limitation of the clock midterm frequency stability. In the Supplemental Material [34], part of the signal optimization and noise analysis for midterm stability are presented in detail.

II. EXPERIMENTAL SETUP

A. Optical setup

Our setup is depicted in Fig. 1. A distributed feedback (DFB) laser diode emits a monochromatic laser beam around 895 nm, the wavelength of the Cs D_1 line. With the help of a fiber electro-optic phase modulator (EOPM), modulated at 4.6 GHz with about 26 dBm microwave power, about 70% of the carrier power is transferred into both first-order sidebands used for CPT interaction. The phase between both optical sidebands, the so-called Raman phase in the following, is further modulated through the driving 4.6-GHz microwave signal. Two acousto-optic modulators (AOMs) are employed. The first one, AOM1, is used for laser power stabilization. The second one, AOM2, allows us to compensate for the buffer-gas-induced optical frequency shift (approximately equal to 160 MHz) in the CPT clock cell. A double-modulated laser beam is obtained by combining the phase modulation with a synchronized polarization modulation performed thanks to a liquid-crystal polarization rotator (LCPR). The laser beam is expanded to an elliptical beam with $1/e^2$ radii of approximately 9 and 16 mm before the vapor cell. The cylindrical Cs vapor cell, 25 mm in diameter and 50 mm long, is filled with 15 Torr of mixed buffer gases (argon and nitrogen). Unless otherwise specified, the cell temperature is stabilized to about 35 °C. A uniform magnetic field of 3.43 μT is applied along the direction of the cell axis by means of a solenoid to remove the Zeeman degeneracy. The ensemble is surrounded by two magnetic shields in order to reject Earth and other stray magnetic fields.

B. Fiber EOPM sideband generation

We first use a Fabry-Perot cavity to investigate the EOPM sideband power ratio versus the coupling 4.596 GHz

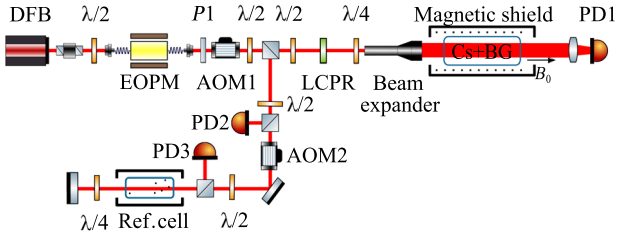

FIG. 1. Optical setup for DM CPT. Distributed feedback diode laser (DFB), electro-optic phase modulator (EOPM), liquid-crystal polarization rotator (LCPR), acousto-optic modulator (AOM), polarizer (P), half- (quarter-) wave plate [$\lambda/2(4)$], buffer gas (BG), photodetector (PD).

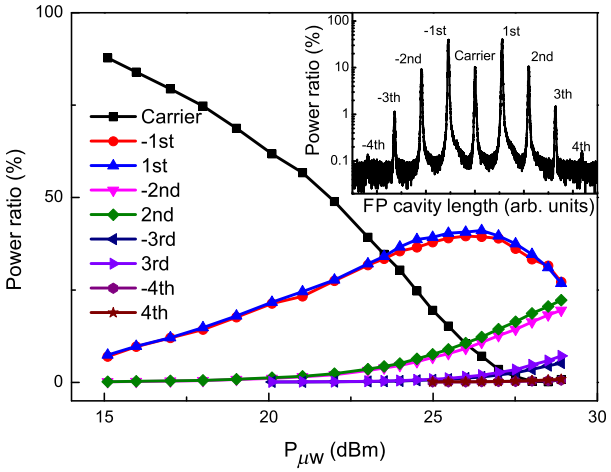

FIG. 2. Fractional power of laser sidebands at the EOPM output as a function of 4.596 GHz microwave power. (Inset) The laser sideband spectrum with $P_{\mu w} = 26.12$ dBm obtained by scanning the Fabry-Perot cavity length; notice the log scale of the y axis.

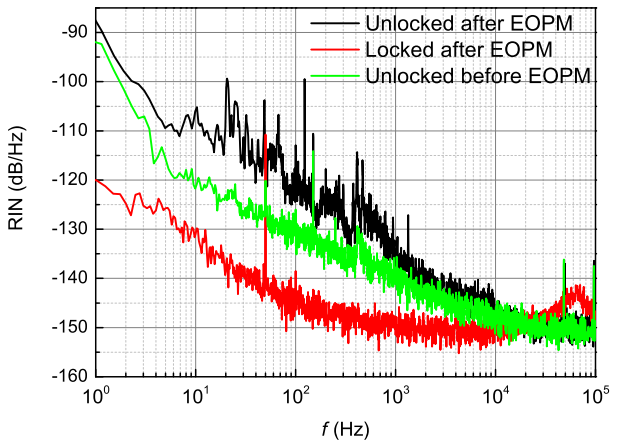

FIG. 3. Power spectral density of the laser RIN with (red) and without (black) power locking after the EOPM, the RIN measured before the EOPM is plotted in green.

microwave power ($P_{\mu w}$); see Fig. 2. We choose $P_{\mu w}$ around 26 dBm to maximize the power-transfer efficiency into the first-order sidebands. The sideband spectrum is depicted in the inset of Fig. 2.

C. Laser power locking

Since the laser intensity noise is known as being one of the main noise sources which limit the performance of a CPT clock [10,31], the laser power needs to be carefully stabilized. For this purpose, a polarization beam splitter (PBS) reflects towards a photodetector (PD) a part of the laser beam, the first order diffracted by AOM1 following the EOPM. The output voltage signal is compared to an ultrastable voltage reference (LT1021). The correction signal is applied on a voltage-variable power attenuator set on the feeding rf power line of the AOM1 with a servo bandwidth of about 70 kHz. The out-loop laser relative intensity noise (RIN) is measured just after the first PBS with a photodetector. The spectrum of the resulting RIN with and without locking is shown in Fig. 3. A 20-dB improvement at $F_M = 125$ Hz [the local-oscillator (LO) modulation frequency for clock operation] is obtained in the stabilized regime.

It is worth noting that the DFB laser diode we used, with a linewidth of about 2 MHz, is sensitive even to the lowest levels of backreflections [37]; e.g., the coated collimated lens may introduce some intensity and frequency noise at the regime of 0.1 to 10 kHz. Finding the correct lens alignment to minimize the reflection-induced noise while keeping a well-collimated laser beam is not an easy task. To reduce light feedback from the EOPM fiber face, we use a 60-dB isolator before the EOPM. Even so, we still find that the EOPM induces additional intensity noise, as reported in Fig. 3 by showing the RIN measured before (in green) and after (in black) the EOPM. Nevertheless, thanks to the laser power locking, we can reduce most of these noises by at least 15 dB in the range of 1 Hz to 1 kHz.

D. Laser-frequency stabilization

Our laser-frequency stabilization setup, similar to that used in Refs. [31,38], is depicted in Fig. 1. We observe in a vacuum cesium cell the two-color Doppler-free spectrum depicted in Fig. 4. The bichromatic beam, linearly polarized, is retroreflected after crossing the cell with the

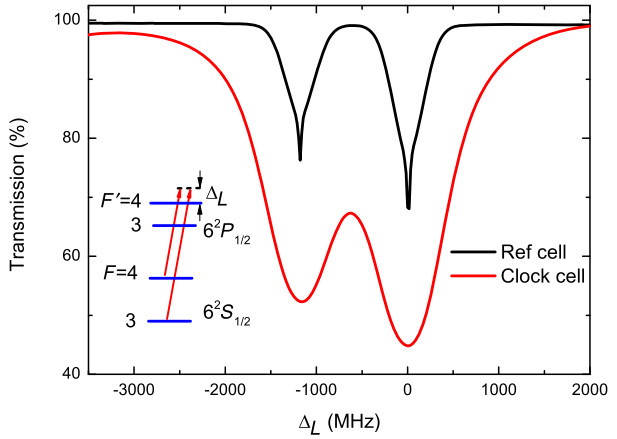

FIG. 4. Spectrum of the Cs D_1 line in the vacuum reference cell and in the clock cell recorded with the bichromatic laser. The optical transitions in the clock cell are broadened and shifted by collisions between the Cs atoms and the buffer-gas molecules. The frequency shift is compensated for by the AOM. The two absorptions from left to right correspond to the excited level $|6^2P_{1/2}, F' = 3\rangle$ and $|6^2P_{1/2}, F' = 4\rangle$, respectively. For the reference cell signal, the laser power is 0.74 mW, the beam diameter 2 mm, the cell temperature 22 °C, and the AOM frequency 160 MHz. (Inset) The atomic levels involved in the D_1 line of cesium.

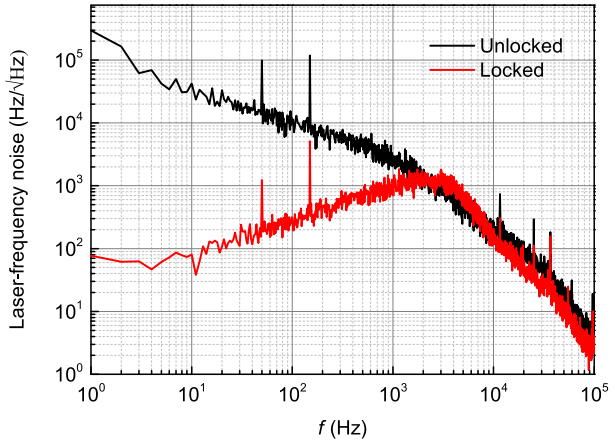

FIG. 5. The laser-frequency noise measured on the error signal of the Doppler-free spectrum with and without frequency locking.

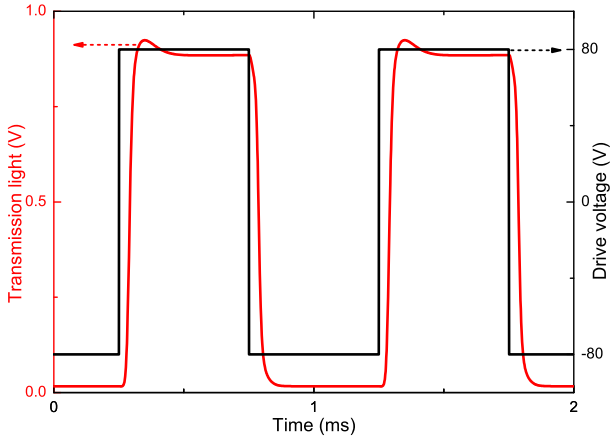

FIG. 6. LCPR response.

orthogonal polarization. Only atoms of a null axial velocity are resonant with both beams. Consequently, CPT states built by a beam are destroyed by the reversed beam, leading to a Doppler-free enhancement of the absorption [38].

The laser-frequency detuning $\Delta_L = 0$ in Fig. 4 corresponds to the laser carrier frequency tuned to the center of both transitions $|6^2S_{1/2}, F = 3\rangle \rightarrow |6^2P_{1/2}, F' = 4\rangle$ and $|6^2S_{1/2}, F = 4\rangle \rightarrow |6^2P_{1/2}, F' = 4\rangle$ in the D_1 line of cesium, where F is the hyperfine quantum number. For the record, the microwave frequency is 4.596 GHz, half the Cs ground-state splitting, and the DFB laser frequency is scanned. We measure the frequency noise by utilizing the error signal of the Doppler-free spectrum as a frequency discriminator, i.e., the power spectral density of the transmission signal at resonance after the reference cell divided by the slope of the error signal at $\Delta_L = 0$. The measured laser-frequency noise is presented in Fig. 5 with and without frequency locking. In the locking case, the servo bandwidth is about 3 kHz and the noise is found to be reduced by about 25 dB at $f = 125$ Hz (the LO modulation frequency in the clock operation).

E. Polarization modulation

We now study the response time of the LCPR (FPR-100-895, Meadowlark Optics). As illustrated in Fig. 6, the measured rise (fall) time is about 100 μs, and the polarization extinction ratio is about 50. By comparison, the electro-optic amplitude modulator (EOAM) used as polarization modulator in our previous investigations [28] showed a response time of 2.5 μs (limited by our high-voltage amplifier) and a polarization extinction ratio of 63. Here, we replace it by a liquid-crystal device because its low voltage and small size would be an ideal choice for a compact CPT clock, and we will show in the following that the longer switching time does not limit the contrast of the CPT signal.

F. Microwave source and clock servo loop

The electronic system (local oscillator and digital electronics for clock operation) used in our experiment is depicted in Fig. 7. The 4.596-GHz microwave source is based on the design described in Ref. [39]. The LO is a module (XM16 Pascall) integrating an ultralow-phase-noise 100-MHz quartz oscillator that is frequency multiplied without excess noise to 1.6 GHz. The 4.596-GHz signal is synthesized by few-frequency multiplication, division, and mixing stages. The frequency modulation and tuning is yielded by a direct digital synthesizer (DDS) referenced to the LO. The clock operation [2,40] is performed by a single field-programmable gate array (FPGA) which coordinates the operation of the DDS, analog-to-digital converters (ADCs), and digital-to-analog converter (DACs).

(1) The DDS generates a signal with phase modulation (modulation rate f_m, depth $\pi/2$) and frequency modulation (F_M, depth Δ_{F_M}).

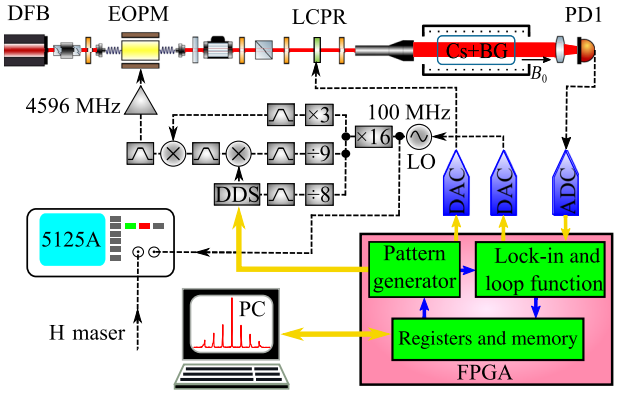

FIG. 7. Electronic architecture of the DM-CPT clock. Direct digital synthesizer (DDS), digital-to-analog converter (DAC) analog-to-digital converter (ADC), field-programmable gate array (FPGA), local oscillator (LO).

(2) The DAC generates a square-wave signal to drive the LCPR with the same rate f_m, synchronous to the phase modulation.
(3) The ADC is the front end of the lock-in amplifier. Another DAC, used to provide the feedback to the local oscillator frequency, is also implemented in the FPGA.

The clock frequency is measured by comparing the LO signal with a 100-MHz signal delivered by a H maser of the laboratory in a Symmetricom 5125A Allan deviation test set. The frequency stability of the maser is 1×10^{-13} at 1 s integration time.

III. CLOCK SIGNAL OPTIMIZATION

A. Time sequence and figure of merit

As illustrated in Fig. 8, the polarization and the phase modulation share the same modulation function. After a pumping time t_d to prepare the atoms for the CPT state, we detect the CPT signal with a window of length t_w. Although the detection is sampled, the interrogation is cw, which is why we call our scheme a cw interrogation scheme. In order to get an error signal to close the clock-frequency loop, the microwave frequency is square-wave modulated with a frequency F_M and a depth Δ_{F_M}. In our case, we choose $F_M = 125$ Hz as a trade-off between a low frequency to have time to accumulate the atomic population in the clock states by the DM scheme and a high operating frequency to avoid low-frequency noise in the lock-in amplification process and diminish the intermodulation effects.

A typical experimental CPT signal, recorded with this time sequence and showing all of the CPT transitions allowed between Zeeman sublevels of the Cs ground state, is reported in Fig. 9. The Raman detuning Δ is the difference between the spacing of the two first sidebands and the Cs clock resonance. The spectrum shows that the clock levels (the 0-0 transition) are the most populated and that the atomic population is symmetrically distributed

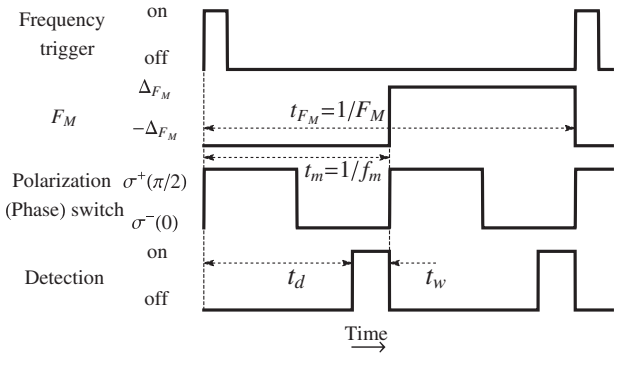

FIG. 8. Time sequence. Modulation frequency of the 4.596 GHz signal (F_M), polarization and phase-modulation frequency (f_m), pumping time (t_d), detection window (t_w).

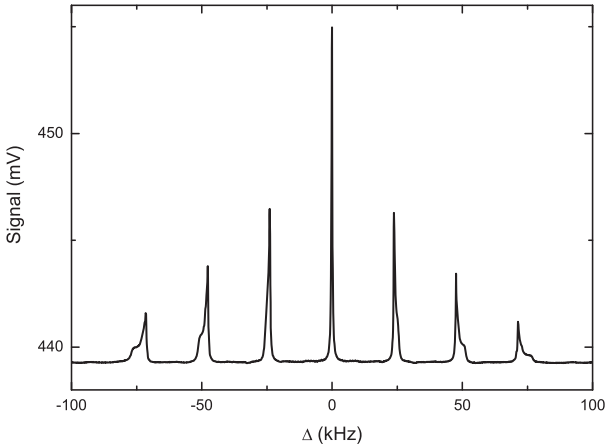

FIG. 9. Zeeman spectrum. The center peak is the 0-0 clock transition. The working parameters are $t_d = 2$ ms, $t_w = 2$ ms, $f_m = 500$ Hz, $P_L = 163$ μW, $P_{\mu w} = 26.12$ dBm, and $T_{\text{cell}} = 35.1$ °C.

around the $(m_F = 0)$ sublevels. The distortion of neighboring lines is explained by magnetic-field inhomogeneities.

It can be shown that the clock short-term frequency stability limited by an amplitude noise scales as W_h/C [10], with W_h being the full width at half maximum (FWHM) of the clock resonance and C the contrast of the resonance. Usually, the ratio of contrast C to W_h is adopted as a figure of merit, i.e., $F_C = C/W_h$. The best stability should be obtained by maximizing F_C.

The stability of the clock is measured by the Allan standard deviation $\sigma_y(\tau)$, with τ being the averaging time. When the signal noise is white, of variance σ_N^2 in 1 Hz bandwidth, and for a square-wave frequency modulation, the stability limited by the signal-to-noise ratio is equal to [41]

$$\sigma_y(\tau) = \frac{1}{f_c}\frac{\sigma_N}{S_\ell}\sqrt{\frac{1}{\tau}}, \tag{1}$$

with f_c being the clock frequency and S_ℓ the slope of the frequency discriminator. In CPT clocks, one of the main sources of noise is the laser intensity noise, which leads to a signal noise proportional to the signal. Therefore, it is more convenient to characterize the quality of the signal of a CPT atomic clock by a new figure of merit, $F_S = S_\ell/V_{wp}$, where S_ℓ is the slope of the error signal (in V/Hz) at Raman resonance ($\Delta = 0$), and V_{wp} is the detected signal value (in volts) at the interrogating frequency (the clock resonance frequency plus the modulation depth Δ_{F_M}); see Fig. 10. Note that an estimation of the discriminator slope is also included in F_C since the contrast is the signal amplitude A divided by the background B. F_C then equals $(A/W_h)/B$, (A/W_h) is a rough approximation of the slope S_ℓ, and B an approximation of the working signal V_{wp}. In our experimental conditions, $A/W_h \sim S_\ell/3$.

We investigate the effect of relevant parameters on both figures of merit to optimize the clock performances. In

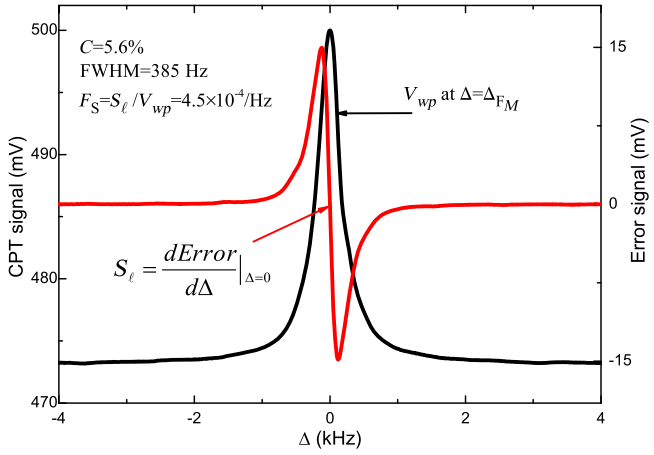

FIG. 10. Signal of the clock transition and error signal. The working parameters are $t_d = 3$ ms, $t_w = 1$ ms, $f_m = 250$ Hz, $P_L = 163$ μW, $P_{\mu w} = 26.12$ dBm, $T_{\text{cell}} = 35.1$ °C.

order to allow a comparison despite different conditions, the error signals are generated with the same unit gain. Since the resonance linewidth is also subject to change, it is necessary to optimize the 4.6-GHz modulation depth Δ_{F_M} to maximize F_S. Here, for simplicity, we first record the CPT signal, and we can then numerically compute the optimized values of Δ_{F_M} and F_S.

In the following, we investigate the dependence of F_C and F_S on several parameters, including the cell temperature (T_{cell}), the laser power (P_L), the microwave power ($P_{\mu w}$), and the polarization (phase-)modulation frequency (f_m). The effects of the detection-window duration (t_w) and the detection start time (t_d) are presented in Figs. 1 and 2, respectively, of the Supplemental Material [34].

B. Cell temperature and laser power

From the figures of merit shown in Fig. 11, the optimized cell temperature is around $T_{\text{cell}} = 35.1$ °C for $P_L = 163$ μW. The narrower linewidth observed at higher

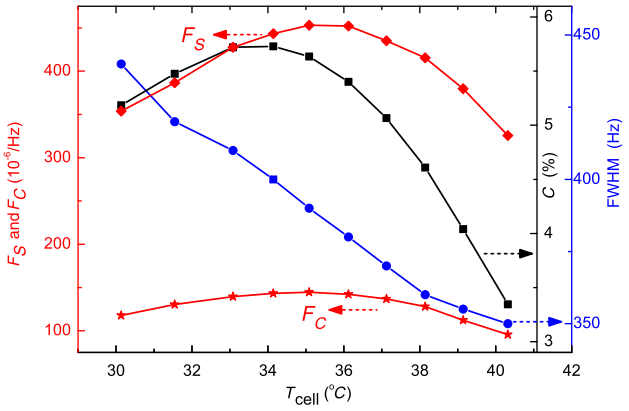

FIG. 11. Figures of merit F_S and F_C, contrast C, and the width of the clock transition as a function of cell temperature T_{cell}. All of the other working parameters are the same as in Fig. 10.

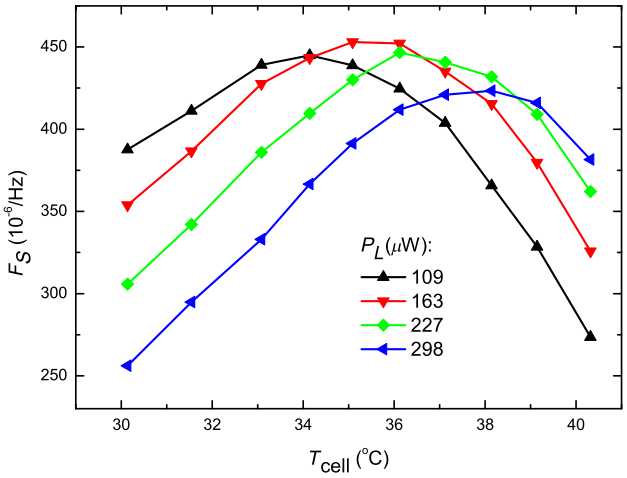

FIG. 12. F_S as a function of cell temperature T_{cell} for various laser powers. All of the other working parameters are the same as in Fig. 10.

T_{cell}, previously observed by Godone *et al.* [42], can be explained by the propagation effect: the higher the cell temperature, the stronger the light absorption by more atoms, and less light intensity is seen by the atoms at the end side of the vapor cell. This effect leads to a reduction of the power broadening and a narrower signal measured by the transmitted light amplitude. The optimum temperature depends on the laser power, as depicted in Fig. 12. Nevertheless, the overall maximum of F_S is reached with $P_L = 163$ μW at $T_{\text{cell}} = 35.1$ °C.

The figures of merit F_S and F_C, the contrast C, and the width are plotted as a function of the laser power in Fig. 13 for $T_{\text{cell}} = 35.1$ °C. The laser powers maximizing F_S and F_C are $P_L = 163$ μW and $P_L = 227$ μW, respectively. The Allan deviation reaches a better value at $P_L = 163$ μW, which justifies our choice of F_S as a figure of merit. In the following parameters investigation, we show only the F_S as a figure of merit for clarity.

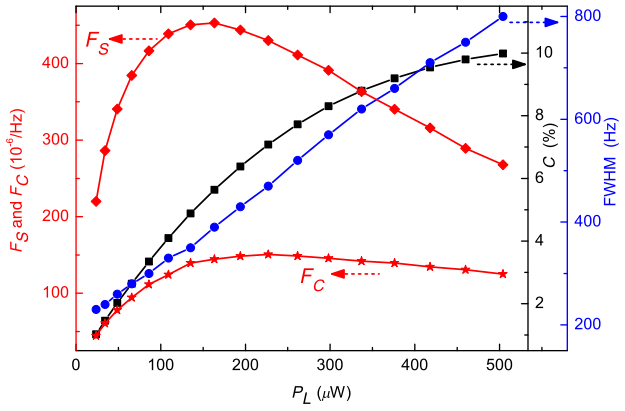

FIG. 13. F_S, F_C, C, and the width of the clock transition as a function of laser power P_L, with $T_{\text{cell}} = 35.1$ °C. All of the other working parameters are the same as in Fig. 10.

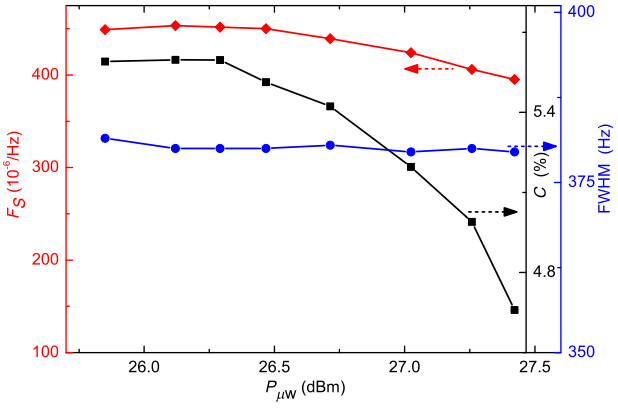

FIG. 14. F_S, C, and the width of the clock transition as a function of microwave power $P_{\mu w}$ with $T_{\text{cell}} = 35.1$ °C. All of the other working parameters are the same as in Fig. 10.

C. Microwave power

F_S, C, and the width versus the microwave power are shown in Fig. 14. The behavior of F_S is basically in agreement with the fractional power of the first (± 1) sidebands of Fig. 2. The optimized microwave power is around 26.12 dBm.

D. Polarization (phase-)modulation frequency f_m

Figure 15 shows F_S, C, and the width versus the polarization (phase-)modulation frequency f_m. The maxima of F_S is reached at a low-frequency f_m. On one hand, this result is an encouraging one that demonstrates the suitability of the LCPR polarization modulator in this experiment. On the other hand, the higher F_M rate would be better for a clock operation with a lock-in method to modulate and demodulate the error signal, to avoid the low-frequency noises such as $1/f$ noise. Therefore, we choose $F_M = 125$ Hz and $f_m = 250$ Hz. We notice that the behavior of C is not exactly the same as the one observed in our previous work [43,44] with a fast EOAM, where the signal amplitude was maximized at higher frequencies. This difference can be explained by the slower response time of the polarization modulator and the lower laser intensity used. The linewidth reaches a minimum around 1.5 kHz. This behavior will be investigated in the future.

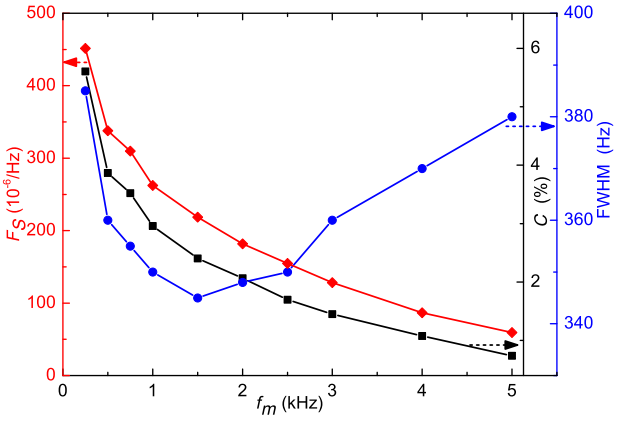

FIG. 15. F_S, C, and the width of the clock transition as a function of f_m. All of the other working parameters are the same as in Fig. 10.

IV. FREQUENCY STABILITY

A. Measured stability

The high contrast and narrow linewidth CPT signal obtained with the optimized values of the parameters is presented in Fig. 10 with the related error signal. The Allan standard deviation of the free-running LO and of the clock frequency, measured against the H maser, are shown in Fig. 16. The former is in agreement with its measured phase noise. In the (1–100)-Hz offset frequency region, the phase-noise spectrum of the free-running 4.596- GHz LO signal is given in dB rad^2/Hz by $S_\varphi(f) = b_{-3}f^{-3}$, with $b_{-3} = -47$, the signature of a flicker frequency noise [39]. This phase noise yields an expected Allan deviation given by $\sigma_y(1s) \approx \sqrt{2\ln 2 \times [(4b_{-3})/f_c^2]} \approx 1.2 \times 10^{-12}$ [45], close to the measured value of 2×10^{-12} at 1 s. The measured stability of the CPT clock is $3.2 \times 10^{-13}\tau^{-1/2}$, up to a 100-s averaging time for our best record. This value is close to the best CPT clocks [31,33], demonstrating that a high-performance CPT clock can be built with the DM-CPT scheme. A typical record for longer averaging times is also shown in Fig. 16. For averaging times τ longer than 20 s, the Allan deviation increases like $\sqrt{\tau}$, signature of a random-walk frequency noise.

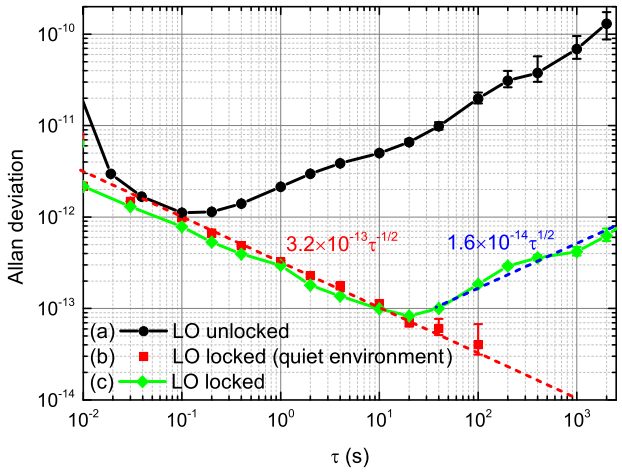

FIG. 16. The LO frequency stability that is (a) free running, (b), (c) locked on the atomic resonance. (b) Best record in a quiet environment. (c) Typical record. The slope of the red (blue) dashed fitted line is $3.2 \times 10^{-13}\tau^{-1/2}$ ($1.6 \times 10^{-14}\tau^{1/2}$).

B. Short-term stability limitations

We have investigated the main noise sources that limit the short-term stability. For a first estimation, we consider only white-noise sources, and, for the sake of simplicity, we assume that the different contributions can independently add, so that the total Allan variance can be computed as

$$\sigma_y^2(\tau) = \Sigma_i \sigma_{y,p_i}^2(\tau) + \sigma_{y,\mathrm{LO}}^2(\tau), \tag{2}$$

with $\sigma_{y,\mathrm{LO}}^2(\tau)$ being the contribution due to the phase noise of the local oscillator, and $\sigma_{y,p_i}^2(\tau)$ the Allan variance of the clock frequency induced by the fluctuations of the parameter p_i. When p_i modifies the clock frequency during the whole interrogation cycle, $\sigma_{y,p_i}^2(\tau)$ can be written as

$$\sigma_{y,p_i}^2(\tau) = \frac{1}{f_c^2}(\sigma_{p_i}^2)_{1\ \mathrm{Hz}}(\delta f_c/\delta p_i)^2 \frac{1}{\tau}, \tag{3}$$

with $(\sigma_{p_i}^2)_{1\ \mathrm{Hz}}$ being the variance of p_i measured in 1 Hz bandwidth at the modulation frequency F_M, $(\delta f_c/\delta p_i)$ is the clock-frequency sensitivity to a fluctuation of p_i. Here, the detection signal is sampled during a time window t_w with a sampling rate $2F_M = 1/T_c$, where T_c is a cycle time. In this case, Eq. (3) becomes

$$\sigma_{y,p_i}^2(\tau) = \frac{1}{f_c^2}(\sigma_{p_i}^2)_{tw}(\delta f_c/\delta p_i)^2 \frac{T_c}{\tau}, \tag{4}$$

with $(\sigma_{p_i}^2)_{tw}$ being the variance of p_i sampled during t_w; $(\sigma_{p_i}^2)_{tw} \approx S_{p_i}(F_M)/(2t_w)$, with $S_{p_i}(F_M)$ being the value of the power spectral density (PSD) of p_i at the Fourier frequency F_M (assuming a white frequency noise around F_M). When p_i induces an amplitude fluctuation with a sensitivity $(\delta V_{wp}/\delta p_i)$, Eq. (4) becomes

$$\sigma_{y,p_i}^2(\tau) = \frac{1}{f_c^2} S_{p_i}(F_M) \frac{(\delta V_{wp}/\delta p_i)^2}{S_\ell^2} \frac{T_c}{2t_w} \frac{1}{\tau}, \tag{5}$$

with S_ℓ being the slope of the frequency discriminator in V/Hz. We review below the contributions of the different sources of noise.

Detector noise.—The square root of the PSD S_d of the signal fluctuations measured in the dark is shown in Fig. 17. It is $N_{\mathrm{detector}} = 64.8\ \mathrm{nV}/\sqrt{\mathrm{Hz}}$ in 1 Hz bandwidth at the Fourier frequency 125 Hz. According to Eq. (5), the contribution of the detector noise to the Allan deviation at 1 s is 0.45×10^{-13}.

Shot noise.—With the transimpedance gain $G_R = 1.5 \times 10^4\ \mathrm{V\,A^{-1}}$ and the detector current $I = V_{wp}/G_R = 32.7\,\mu\mathrm{A}$, Eq. (5) becomes

$$\sigma_{y,\mathrm{sh}}^2(\tau) = \frac{1}{f_c^2} \frac{(2eIG_R)^2}{S_\ell^2} \frac{T_c}{2t_w} \frac{1}{\tau}, \tag{6}$$

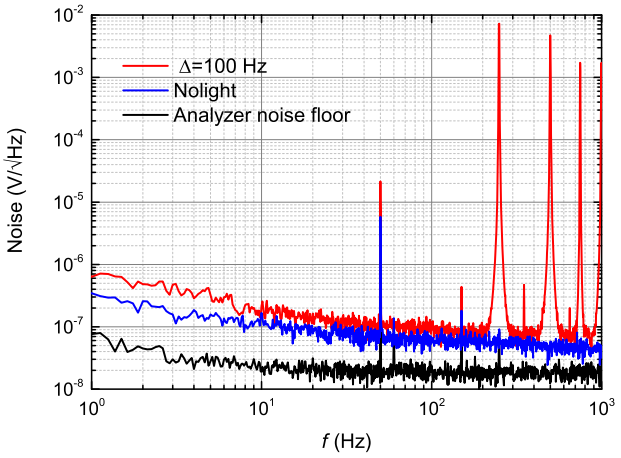

FIG. 17. The RIN after the cell, detector noise, and analyzer noise floor. The working parameters are the same as in Fig. 10.

with e being the electron charge. The contribution to the Allan deviation at 1 s is 0.34×10^{-13}.

Laser frequency-modulation to amplitude-modulation (FM-AM) noise: it is the amplitude noise induced by the laser carrier frequency noise. The slope of the signal V_{wp} with respect to the laser frequency f_L is $S_{\text{FM-AM}} = 0.16\ \mathrm{mV\,MHz^{-1}}$ at optical resonance. According to Eq. (5), with data from the laser-frequency-noise PSD of Fig. 5 at 125 Hz, we get an Allan deviation of 0.33×10^{-13} at 1 s.

Laser AM-AM noise.—This noise is defined as the amplitude noise induced by the laser intensity noise. The measured signal sensitivity to the laser power is $S_{\mathrm{AM}} = 3.31\ \mathrm{mV}\,\mu\mathrm{W^{-1}}$ at $P_L = 163\ \mu\mathrm{W}$, combined with the laser intensity PSD of Fig. 3 it leads to the amplitude noise $S_{\mathrm{AM}} \times P_L \times \mathrm{RIN}(125\ \mathrm{Hz}) = 30.3\ \mathrm{nV}/\sqrt{\mathrm{Hz}}$, and an Allan deviation of 0.21×10^{-13} at 1 s.

LO phase noise.—The phase noise of the local oscillator degrades the short-term frequency stability via the intermodulation effect [46]. It can be estimated by

$$\sigma_{y_{\mathrm{LO}}}(1s) \sim \frac{F_M}{f_c} \sqrt{S_\varphi(2F_M)}. \tag{7}$$

Our 4.596-GHz microwave source is based on Ref. [39], which shows an ultralow phase noise $S_\varphi(2F_M) = -116\ \mathrm{dB\,rad^2\,Hz^{-1}}$ at $2F_M = 250$ Hz Fourier frequency. This value yields a contribution to the Allan deviation of 0.43×10^{-13} at 1 s.

Microwave-power noise.—Fluctuations of microwave power lead to a laser intensity noise, which is already taken into account in the RIN measurement. We show in the next section that they also lead to a frequency shift (see Fig. 20). The Allan deviation of the microwave power at 1s is 2.7×10^{-4} dBm; see the inset of Fig. 20. With a measured slope of 7.7 Hz/dBm, we get a fractional-frequency Allan deviation of 2.26×10^{-13}, which is the largest contribution to

TABLE I. Noise contributions to the stability at 1 s.

Noise source	Noise level	$\sigma_y(1s) \times 10^{13}$
Detector noise	64.8 nV/$\sqrt{\text{Hz}}$	0.45
Shot noise	48.8 nV/$\sqrt{\text{Hz}}$	0.34
Laser FM-AM	48.0 nV/$\sqrt{\text{Hz}}$	0.33
Laser AM-AM	30.3 nV/$\sqrt{\text{Hz}}$	0.21
LO phase noise	-116 dB rad^2/Hz	0.43
$P_{\mu w}$	2.7×10^{-4} dBm at 1s	2.26
Laser AM-FM	0.6 nW at 1s	9.7×10^{-3}
Laser FM-FM	approximately 100 Hz at 1s	2.9×10^{-3}
T_{cell}	6.3×10^{-5} K at 1s	3.2×10^{-2}
B_0	4.3 pT at 1s	1.4×10^{-3}
Total		2.4

the stability at 1 s. Note that, in our setup, the microwave power is not stabilized.

The other noise sources considered have much lower contributions: they are the laser-frequency-shift effect, i.e., AM-FM and FM-FM contributions, the cell temperature, and the magnetic field. Table I resumes the short-term stability noise budget.

The laser intensity noise after interacting with the atomic vapor is depicted in Fig. 17. It encloses the different contributions to the amplitude noise, i.e., the detector noise, the shot noise, and the FM-AM and AM-AM noises. The noise spectral density is 100 nV/$\sqrt{\text{Hz}}$ at the Fourier frequency 125 Hz, which leads to an Allan deviation of 0.7×10^{-13} at 1 s. This value is equal to the quadratic sum of the individual contributions. The quadratic sum of all of the noise contributions leads to an Allan deviation at 1 s of 2.4×10^{-13}, while the measured stability is $3.2 \times 10^{-13}\tau^{-1/2}$ (Fig. 16). The discrepancy could be explained by correlations between different noises, which are not all independent. The dominant contribution is the clock-frequency shift induced by the microwave-power fluctuations. This term could be reduced by microwave-power stabilization or a well-chosen laser power (see Fig. 14), but to the detriment of the signal amplitude.

V. FREQUENCY SHIFTS AND MIDTERM STABILITY

We have investigated the clock-frequency shift f_0 with respect to the variation of various parameters, with the definition $f_0 = f_c - f_{\text{Cs}}$, f_{Cs} is the unperturbed Cs atomic-clock frequency 9.192 631770 GHz. Here, we address the polarization (phase-)modulation frequency f_m, the laser power P_L, and the microwave power $P_{\mu w}$ induced clock-frequency shift. The other parameter measurements can be found in Figs. 3–5 in the Supplemental Material [34]. For each frequency measurement, the LO frequency is locked on the CPT resonance. With a 100-s averaging time, the mean frequency is measured with a typical error bar less than 10^{-12}, i.e., 0.01 Hz relative to the Cs frequency f_{Cs}.

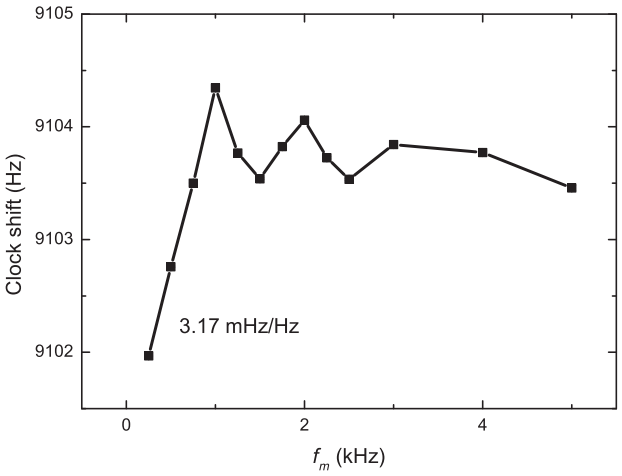

FIG. 18. Clock frequency as a function of the polarization (phase-)modulation frequency f_m. All of the other working parameters are the same as in Fig. 10.

A. f_0 versus f_m

In order to gain more insight into the physics involved in our experiment, we measure the clock shift versus the polarization (phase-)modulation frequency f_m. The results are reported in Fig. 18. The oscillatory behavior is not fully understood yet; we are going to investigate it theoretically by taking into consideration the slow response time [43] of our LCPR in the future. When other parameters are fixed, the shift coefficient is 3.17 mHz Hz^{-1} at $f_m = 250$ Hz. As f_m is synchronized to the LO, which exhibits, in the worst case (unlocked), a frequency stability at the level of 7×10^{-11} at 1000 s (see Fig. 16), the effect of the polarization and the phase-modulation frequency on the clock shift is negligible, i.e., 6.0×10^{-21} at 1000 s.

B. f_0 versus P_L

The clock-frequency shift versus P_L is presented in Fig. 19. The coefficient of the light-power shift is 14.9 Hz mW^{-1} at $P_L = 163$ μW and $P_{\mu w} = 26.12$ dBm. This shift is difficult to foresee theoretically because it results not only from the combination of light shifts (the ac Stark shift) induced by all sidebands of the optical spectrum but also from the overlapping and broadening of neighboring lines [35,36]. The inset of Fig. 19 shows the typical fractional fluctuations of the laser power versus the integration time. They are measured to be 1×10^{-4} at 1000 s, impacting on the clock fractional-frequency stability at the level of 2.6×10^{-14} at 1000 s. Since the power distribution in the sidebands vary with the microwave power, the laser power shift is also sensitive to the microwave-power feeding the EOPM. This sensitivity is clearly shown in Fig. 19. As previously observed in CPT-based clocks [47,48] and double-resonance Rb clocks [49], it is important to note that the light-power shift coefficient can

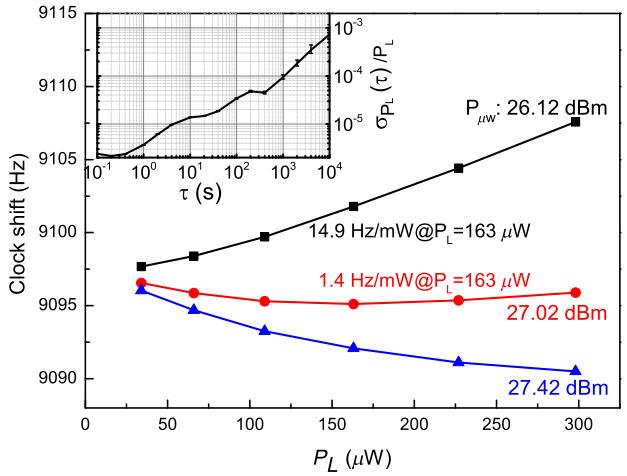

FIG. 19. Clock frequency as a function of the laser power P_L for different values of $P_{\mu w}$. (Inset) Fractional Allan deviation of the laser power. All of the other working parameters are the same as in Fig. 10.

be decreased and even canceled at specific values of $P_{\mu w}$. Consequently, it should be possible to improve the long-term frequency stability by tuning finely the microwave-power value [50,51], at the expense of a slight degradation of the short-term frequency stability.

C. f_0 versus $P_{\mu w}$

The frequency shift versus the microwave power at various levels of laser power is shown in Fig. 20. At constant optical power, only the power distribution among the different sideband changes. The shift scales as the microwave power in the investigated range, with a sensitivity of

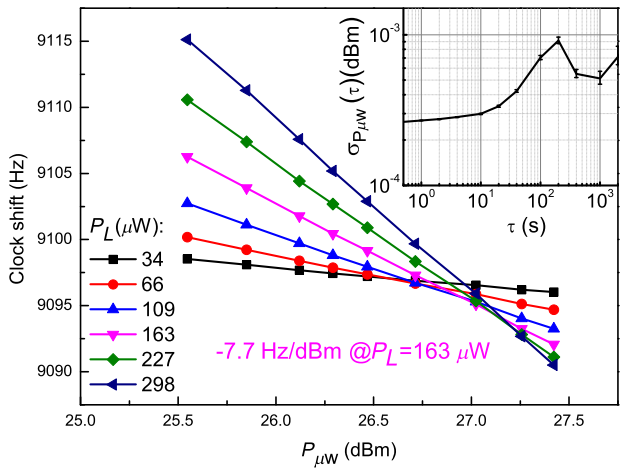

FIG. 20. Clock frequency as a function of the microwave power $P_{\mu w}$ at various levels of laser power. (Inset) Allan deviation of the microwave power in dBm, log scale. All of the other working parameters are the same as in Fig. 10.

TABLE II. Noise contributions to the stability at 1000 s.

Parameter	Coefficient	$\sigma_y(1000s) \times 10^{13}$
T_{cell}	0.47 Hz K^{-1}	2.7×10^{-2}
P_L	14.9 Hz mW^{-1}	0.26
$P_{\mu w}$	−7.7 Hz dBm^{-1}	4.2
Δ_L	−26.6 mHz MHz^{-1}	0.14
B_0	0.29 Hz μT^{-1}	0.4×10^{-2}
Total		4.2

7.7 Hz dBm^{-1} at $P_L = 163$ μW. In this range, the power ratio of both first (± 1) sidebands changes by about 10%. The inset of Fig. 20 shows the Allan deviation of the microwave power in dBm. The typical microwave-power standard deviation of 5×10^{-4} dBm at 1000 s yields a fractional-frequency stability of about 4.2×10^{-13} at 1000 s.

D. Midterm stability

With the shift coefficients and the Allan standard deviation of the involved parameters, we can estimate the various contributions to the midterm clock-frequency stability. They are listed in Table II for a 1000-s averaging time. Their quadratic sum leads to a frequency stability of 4.2×10^{-13} at $\tau = 1000$ s, in very good agreement with the measured stability of 4.21×10^{-13} (see Fig. 16). Again, the main contribution to the instability comes from the microwave-power fluctuations, before the laser power and frequency fluctuations. Thus, in the future, it will be necessary to stabilize the microwave power to improve both the short- and midterm frequency stabilities.

VI. CONCLUSIONS

In this article, we implement a compact vapor-cell atomic clock based on the DM-CPT technique. A detailed characterization of the CPT resonance versus several experimental parameters is performed. A clock-frequency stability of $3.2 \times 10^{-13}\tau^{-1/2}$, up to a 100-s averaging time, is demonstrated. For longer averaging times, the Allan deviation scales as $\sqrt{\tau}$, the signature of a random-walk frequency noise. It has been highlighted that the main limitation to the clock short and midterm frequency stability is the fluctuations of the microwave power feeding the EOPM. Improvements could be achieved by implementing a microwave-power stabilization. Another or a complementary solution could be to choose a finely tuned laser power value minimizing the microwave-power sensitivity. This adjustment could be at the expense of the signal reduction, and a trade-off has to be found. Nevertheless, the recorded short-term stability is already at the level of the best CPT clocks [31,33] and close to state-of-the-art Rb vapor-cell frequency standards. These preliminary results show the possibility to a high-performance and compact CPT clock based on the DM-CPT technique.

ACKNOWLEDGMENTS

We thank Moustafa Abdel Hafiz (FEMTO-ST) and David Holleville and Luca Lorini (LNE-SYRTE) for the helpful discussions. We are also pleased to acknowledge Charles Philippe and Ouali Acef for supplying the thermal-insulation material, Michel Abgrall for lending the Symmetricom 5125A instrument, David Horville for the laboratory arrangement, José Pinto Fernandes, Michel Lours for the electronic assistance, Pierre Bonnay, and Annie Gérard for manufacturing the Cs cells. P. Y. is supported by CNRS. This work is supported in part by ANR and DGA (ISIMAC Project No. ANR-11-ASTR-0004). This work has been funded by the EMRP program (IND55 Mclocks). The EMRP is jointly funded by the EMRP-participating countries within EURAMET and the European Union.

[1] J. Camparo, The rubidium atomic clock and basic research, Phys. Today **60**, No. 11, 33 (2007).
[2] S. Micalizio, C. E. Calosso, A. Godone, and F. Levi, Metrological characterization of the pulsed Rb clock with optical detection, Metrologia **49**, 425 (2012).
[3] T. Bandi, C. Affolderbach, C. Stefanucci, F. Merli, A. K. Skrivervik, and G. Mileti, Compact high-performance continuous-wave double-resonance rubidium standard with $1.4 \times 10^{-13}\tau^{-1/2}$ stability, IEEE Trans. Ultrason. Ferroelectr. Freq. Control **61**, 1769 (2014).
[4] S. Kang, M. Gharavipour, C. Affolderbach, F. Gruet, and G. Mileti, Demonstration of a high-performance pulsed optically pumped Rb clock based on a compact magnetron-type microwave cavity, J. Appl. Phys. **117**, 104510 (2015).
[5] A. Godone, F. Levi, C. E. Calosso, and S. Micalizio, High-performing vapor cell frequency standards, Riv. Nuovo Cimento **38**, 133 (2015).
[6] G. Alzetta, A. Gozzini, L. Moi, and G. Orriols, An experimental method for the observation of r.f. transitions and laser beat resonances in oriented Na vapour, Nuovo Cimento Soc. Ital. Fis. **36B**, 5 (1976).
[7] E. Arimondo, Coherent population trapping in laser spectroscopy, Prog. Opt. **35**, 257 (1996).
[8] K. Bergmann, H. Theuer, and B. W. Shore, Coherent population transfer among quantum states of atoms and molecules, Rev. Mod. Phys. **70**, 1003 (1998).
[9] R. Wynands and A. Nagel, Precision spectroscopy with coherent dark states, Appl. Phys. B **68**, 1 (1999).
[10] J. Vanier, Atomic clocks based on coherent population trapping: A review, Appl. Phys. B **81**, 421 (2005).
[11] M. Bajcsy, A. S. Zibrov, and M. D. Lukin, Stationary pulses of light in an atomic medium, Nature (London) **426**, 638 (2003).
[12] P. D. D. Schwindt, S. Knappe, V. Shah, L. Hollberg, J. Kitching, L. A. Liew, and J. Moreland, Chip-scale atomic magnetometer, Appl. Phys. Lett. **85**, 6409 (2004).
[13] E. Breschi, Z. D. Gruji, P. Knowles, and A. Weis, A high-sensitivity push-pull magnetometer, Appl. Phys. Lett. **104**, 023501 (2014).
[14] A. Aspect, E. Arimondo, R. Kaizer, N. Vansteenkiste, and C. Cohen-Tannoudji, Transient velocity-selective coherent population trapping in one dimension, J. Opt. Soc. Am. B **6**, 2112 (1989).
[15] J. Vanier and C. Mandache, The passive optically pumped Rb frequency standard: The laser approach, Appl. Phys. B **87**, 565 (2007).
[16] J. E. Thomas, S. Ezekiel, C. C. Leiby, R. H. Picard, and C. R. Willis, Ultrahigh-resolution spectroscopy and frequency standards in the microwave and far-infrared regions using optical lasers, Opt. Lett. **6**, 298 (1981).
[17] J. E. Thomas, P. R. Hemmer, S. Ezekiel, C. C. Leiby, Jr., R. H. Picard, and C. R. Willis, Observation of Ramsey Fringes Using a Stimulated, Resonance Raman Transition in a Sodium Atomic Beam, Phys. Rev. Lett. **48**, 867 (1982).
[18] N. Cyr, M. Tetu, and M. Breton, All-optical microwave frequency standard—A proposal, IEEE Trans. Instrum. Meas. **42**, 640 (1993).
[19] J. Kitching, N. Vukicevic, L. Hollberg, S. Knappe, R. Wynands, and W. Weidemann, A microwave frequency reference based on VCSEL-driven dark line resonances in Cs vapor, IEEE Trans. Instrum. Meas. **49**, 1313 (2000).
[20] J. Kitching, L. Hollberg, S. Knappe, and R. Wynands, Compact atomic clock based on coherent population trapping, Electron. Lett. **37**, 1449 (2001).
[21] J. Kitching, S. Knappe, and L. Hollberg, Miniature vapor-cell atomic-frequency references, Appl. Phys. Lett. **81**, 553 (2002).
[22] L. Liew, S. Knappe, J. Moreland, H. Robinson, L. Hollberg, and J. Kitching, Microfabricated alkali atom vapor cells, Appl. Phys. Lett. **84**, 2694 (2004).
[23] S. Knappe, V. Shah, P. D. D. Schwindt, L. Hollberg, J. Kitching, L.-A.Liew, and J. Moreland, A microfabricated atomic clock, Appl. Phys. Lett. **85**, 1460 (2004).
[24] See http://www.microsemi.com/products/timing-synchronizationsystems/embedded-timing-solutions/components/sa-45s-chip-scale-atomic-clock#resources.
[25] See http://www.inrim.it/Mclocks.
[26] V. Shah and J. Kitching, in *Advances in Atomic, Molecular, and Optical Physics*, Vol. 59, edited by E. Arimondo, P. R. Berman, and C. C. Lin (Elsevier, Amsterdam, 2010).
[27] Peter Yun, Ph.D. thesis, Wuhan Institute of Physics and Mathematics Chinese Academy of Sciences, 2012.
[28] P. Yun, J.-M. Danet, D. Holleville, E. de Clercq, and S. Guérandel, Constructive polarization modulation for coherent population trapping clock, Appl. Phys. Lett. **105**, 231106 (2014).
[29] Y.-Y. Jau, E. Miron, A. B. Post, N. N. Kuzma, and W. Happer, Push-Pull Optical Pumping of Pure Superposition States, Phys. Rev. Lett. **93**, 160802 (2004).
[30] X. Liu, J.-M. Mérolla, S. Guérandel, C. Gorecki, E. de Clercq, and R. Boudot, Coherent population trapping resonances in buffer-gas-filled Cs-vapor cells with push-pull optical pumping, Phys. Rev. A **87**, 013416 (2013).
[31] M. Abdel Hafiz and R. Boudot, A coherent population trapping Cs vapor cell atomic clock based on push-pull optical pumping, J. Appl. Phys. **118**, 124903 (2015).
[32] T. Zanon, S. Guérandel, E. de Clercq, D. Holleville, N. Dimarcq, and A. Clairon, High Contrast Ramsey Fringes with Coherent-Population-Trapping Pulses in a Double

Lambda Atomic System, Phys. Rev. Lett. **94**, 193002 (2005).
[33] J.-M. Danet, O. Kozlova, P. Yun, S. Guérandel, and E. de Clercq, Compact atomic clock prototype based on coherent population trapping, EPJ Web Conf. **77**, 00017 (2014).
[34] See Supplemental Material at http://link.aps.org/supplemental/10.1103/PhysRevApplied.7.014018 for additional parameter measurement results, which in includes Refs. [35,36].
[35] O. Kozlova, S. Guérandel, and E. de Clercq, Temperature and pressure shift of the Cs clock transition in the presence of buffer gases: Ne, N_2, Ar, Phys. Rev. A **83**, 062714 (2011).
[36] O. Kozlova, J.-M. Danet, S. Guérandel, and E. de Clercq, Limitations of long-term stability in a coherent population trapping Cs clock, IEEE Trans. Instrum. Meas. **63**, 1863 (2014).
[37] R. Schmeissner, N. von Bande, A. Douahi, O. Parillaud, M. Garcia, M. Krakowski, and M. Baldy, in *Proceedings of the 2016 European Frequency and Time Forum*, http://www.eftf.org/previousmeetings.php.
[38] M. Abdel Hafiz, G. Coget, E. De Clercq, and R. Boudot, Doppler-free spectroscopy on the Cs D_1 line with a dual-frequency laser, Opt. Lett. **41**, 2982 (2016).
[39] B. François, C. E. Calosso, M. Abdel Hafiz, S. Micalizio, and R. Boudot, Simple-design ultra-low phase noise microwave frequency synthesizers for high-performing Cs and Rb vapor-cell atomic clocks, Rev. Sci. Instrum. **86**, 094707 (2015).
[40] C. E. Calosso, S. Micalizio, A. Godone, E. K. Bertacco, and F. Levi, Electronics for the pulsed rubidium clock: Design and characterization, IEEE Trans. Ultrason. Ferroelectr. Freq. Control **54**, 1731 (2007).
[41] J. Vanier and C. Audoin, *The Quantum Physics of Atomic Frequency Standards* (Adam Hilger, Bristol, 1989).
[42] A. Godone, F. Levi, S. Micalizio, and J. Vanier, Dark-line in optically-thick vapors: Inversion phenomena and line width narrowing, Eur. Phys. J. D **18**, 5 (2002).
[43] P. Yun, S. Guérandel, and E. de Clercq, Coherent population trapping with polarization modulation, J. Appl. Phys. **119**, 244502 (2016).
[44] P. Yun, S. Mejri, F. Tricot, M. Abdel Hafiz, R. Boudot, E. de Clercq, and S. Guérandel, Double-modulation *CPT* cesium compact clock, J. Phys. Conf. Ser. **723**, 012012 (2016).
[45] Enrico Rubiola, *Phase Noise and Frequency Stability in Oscillators* (Cambridge University Press, Cambridge, England, 2009).
[46] C. Audoin, V. Candelier, and N. Dimarcq, A limit to the frequency stability of passive frequency standards due to an intermodulation effect, IEEE Trans. Instrum. Meas. **40**, 121 (1991).
[47] F. Levi, A. Godone, and J. Vanier, The light-shift effect in the coherent population trapping cesium maser, IEEE Trans. Ultrason. Ferroelectr. Freq. Control **47**, 466 (2000).
[48] M. Zhu and L. S. Cutler, in *Proceedings of the 32nd Precise Time and Time Interval Systems and Applications Meeting, Reston, VA, 2000*, edited by L. A. Breakiron (US Naval Observatory, Washington, DC, 2000), p. 311.
[49] C. Affolderbach, C. Andreeva, S. Cartaleva, T. Karaulanov, G. Mileti, and D. Slavov, Light-shift suppression in laser optically pumped vapour-cell atomic frequency standards, Appl. Phys. B **80**, 841 (2005).
[50] V. Shah, V. Gerginov, P. D. D. Schwindt, S. Knappe, L. Hollberg, and J. Kitching, Continuous light-shift correction in modulated coherent population trapping clocks, Appl. Phys. Lett. **89**, 151124 (2006).
[51] B. H. McGuyer, Y. Y. Jau, and W. Happer, Simple method of light-shift suppression in optical pumping systems, Appl. Phys. Lett. **94**, 251110 (2009).